eprints@whiterose.ac.uk
https://eprints.whiterose.ac.uk/

Modulated patterns in a reduced model of a transitional shear flow

C. Beaume[1,2], E. Knobloch[3], G. P. Chini[4], K. Julien[5]

[1]*Department of Aeronautics, Imperial College London, London SW7 2AZ, UK*

[2]*Department of Applied Mathematics, University of Leeds, Leeds LS2 9JT, UK*

[2]*Department of Physics, University of California, Berkeley CA 94720, USA*

[3]*Department of Mechanical Engineering & Program in Integrated Applied Mathematics,*

University of New Hampshire, Durham NH 03824, USA

[4]*Department of Applied Mathematics, University of Colorado, Boulder CO 80309, USA*

Abstract

We consider a close relative of plane Couette flow called Waleffe flow in which the fluid is confined between two free-slip walls and the flow driven by a sinusoidal force. We use a reduced model of such flows constructed elsewhere to compute stationary exact coherent structures of Waleffe flow in periodic domains with a large spanwise period. The computations reveal the emergence of stationary states exhibiting strong amplitude and wavelength modulation in the spanwise direction. These modulated

states lie on branches exhibiting complex dependence on the Reynolds number but
no homoclinic snaking.

PACS numbers: 02.40.-k, 12.39.Dc, 14.80.Hv

1   Introduction

Many parallel shear flows are characterised by a laminar unidirectional flow state that is
linearly stable regardless of the value of the Reynolds number $Re \equiv UL/\nu$, where U is
a typical flow speed, L is a characteristic length scale and ν is the kinematic viscosity of
the fluid. Despite the stability of the laminar flow, experiments and numerical simulations
invariably reveal the presence of turbulence at large values of Re. Unlike fully developed
turbulent flows, transitional parallel shear flows are characterised by the importance of
exact coherent structures (ECS): patterned stationary or time-periodic states that are exact
solutions of the Navier–Stokes equations. These ECS are formed at moderate values of the
Reynolds number, $Re = O(100)$, through saddle-node bifurcations and are characterized
by a small number of unstable eigendirections. As a result, they attract transitional flow
trajectories which can then be thought of as bouncing from ECS to ECS [12, 17]. Of
these, two specific ECS are of particular interest in small domains: the least unstable
lower branch solution and the associated upper branch solution. The lower branch ECS
are typically attractors on the separatrix between the stable laminar unidirectional flow
and the attracting turbulent state and are referred to as edge states [23]. As the Reynolds
number increases, the energy of this states decreases and the basin of attraction of the
laminar state shrinks in favor of that of turbulence. On the other hand, the upper branch
ECS are known to reproduce important low-order statistics of the turbulent flow associated
with it [28, 16]. Numerous other ECS have been found all of which have a small number of
unstable eigendirections. Together these states form a highly complex network that acts as

a backbone of turbulence in small domains [12]. The situation in large domains is naturally more complicated, although simulations have provided some insight, notably into spatially extended edge states [11, 25].

In small domain plane Couette flow, edge states can be decomposed into Fourier modes in the streamwise direction and continued to higher values of the Reynolds number to reveal a characteristic scaling with inverse powers of the Reynolds number [29], confirming earlier scaling theory [26, 13, 27]. This particular ECS consists of a streamwise-invariant streamwise velocity mode that remains $O(1)$ at all values of Re: the *streaks*. These are complemented with *rolls*, a streamwise-invariant vorticity/streamfunction mode whose amplitude decays like Re^{-1}, and *fluctuations*, i.e., the streamwise dependent part of the solution that decays roughly like $Re^{-0.9}$. In this paper, we use a reduced model based on this scaling derived by Beaume *et al.* [2, 5] to calculate spatially extended ECS in the spanwise direction. In the next section, we introduce the reduced model, followed in section 3 by a description of the new ECS computed in a moderately large domain. The paper ends with a brief conclusion.

2   Reduced model

We consider Waleffe flow in which a fluid confined between two parallel stationary stress-free walls is driven by a streamwise-invariant volume force varying sinusoidally with the wall-normal direction, $\mathbf{f} = \frac{\sqrt{2}\pi^2}{4Re}\sin(\frac{\pi y}{2})\hat{\mathbf{x}}$, where $y \in [-1, 1]$. The streamwise $\hat{\mathbf{x}}$ and spanwise $\hat{\mathbf{z}}$ directions are considered periodic. This flow was first introduced by Drazin & Reid as an exception to Rayleigh's inflection point theorem [10]. It has also been used by Waleffe as an analogy to plane Couette flow that makes it possible to project solutions onto a small set of Fourier modes [27]. The flow was recently used to motivate the reduced model [5] used here and shown to display qualitatively the same physics as plane Couette flow

but without the boundary layers present in Couette flow [5, 8]. As emphasized below the reduced model that results is independent of the specific choice of base flow.

The Reynolds number scaling of the lower branch solutions observed in plane Couette flow [29] can be used as part of a multiscale analysis by introducing the small quantity $\epsilon = Re^{-1} \ll 1$ and a slow time scale $T = \epsilon t$. The incompressible Navier–Stokes equation for Waleffe flow then takes the form

$$(\partial_t + \epsilon \partial_T)\,\mathbf{u} + (\mathbf{u} \cdot \nabla)\,\mathbf{u} = -\nabla p + \epsilon \nabla^2 \mathbf{u} + \epsilon \frac{\sqrt{2}\pi^2}{4} \sin\left(\frac{\pi y}{2}\right) \hat{\mathbf{x}}, \tag{1}$$

$$\nabla \cdot \mathbf{u} = 0, \tag{2}$$

where $\mathbf{u} = (u, v, w)$ is the velocity field and p the pressure. The following expansion is assumed:

$$u(x, y, z, t, T) \sim \overline{u}_0(y, z, T) + \epsilon \left[\overline{u}_1(y, z, T) + u_1'(y, z, t, T)e^{i\alpha x} + c.c.\right] + O(\epsilon^2), \tag{3}$$

$$v(x, y, z, t, T) \sim \epsilon \left[\overline{v}_1(y, z, T) + v_1'(y, z, t, T)e^{i\alpha x} + c.c.\right] + O(\epsilon^2), \tag{4}$$

$$w(x, y, z, t, T) \sim \epsilon \left[\overline{w}_1(y, z, T) + w_1'(y, z, t, T)e^{i\alpha x} + c.c.\right] + O(\epsilon^2), \tag{5}$$

with p expanded analogously to ensure incompressibility. In writing these expressions, we have used the numerical observation of Wang *et al.* [29] and introduced the stream-wise wavenumber α. The quantities with an overline represent streamwise-invariant quantities while primed quantities represent fluctuations about this mean state. Note that streamwise-invariant quantities do not vary with the (fast) time t [5].

4

Using these expansions in equations (1) and (2), and averaging over x and t, we obtain:

$$\partial_T \overline{u}_0 + (\overline{\mathbf{v}}_{\mathbf{1}\perp} \cdot \nabla_\perp) \overline{u}_0 = \nabla_\perp^2 \overline{u}_0 + \tfrac{\sqrt{2}\pi^2}{4} \sin\left(\tfrac{\pi y}{2}\right), \tag{6}$$

$$\partial_T \overline{\mathbf{v}}_{\mathbf{1}\perp} + \nabla_\perp \cdot \left[\overline{\mathbf{v}}_{\mathbf{1}\perp}\overline{\mathbf{v}}_{\mathbf{1}\perp} + \overline{\mathbf{v}'_{\mathbf{1}\perp}\mathbf{v}'_{\mathbf{1}\perp}}\right] = -\nabla_\perp \overline{p}_2 + \nabla_\perp^2 \overline{\mathbf{v}}_{\mathbf{1}\perp}, \tag{7}$$

$$\nabla_\perp \cdot \overline{\mathbf{v}}_{\mathbf{1}\perp} = 0, \tag{8}$$

where $\overline{\mathbf{v}}_{\mathbf{1}\perp} \equiv (\overline{v}_1, \overline{w}_1)$, $\mathbf{v}'_{\mathbf{1}\perp} \equiv (v'_1, w'_1)$, $\nabla_\perp \equiv (\partial_y, \partial_z)$; $\overline{\mathbf{v}'_{\mathbf{1}\perp}\mathbf{v}'_{\mathbf{1}\perp}}$ denotes the (x, t)-average of the product of the fluctuations. The fluctuations in turn obey a set of quasilinear equations obtained by substracting the above system to the Navier–Stokes equations:

$$\partial_t u'_1 + i\alpha \overline{u}_0 u'_1 + (\mathbf{v}'_{\mathbf{1}\perp} \cdot \nabla_\perp) \overline{u}_0 = -i\alpha p'_1, \tag{9}$$

$$\partial_t \mathbf{v}'_{\mathbf{1}\perp} + i\alpha \overline{u}_0 \mathbf{v}'_{\mathbf{1}\perp} = -\nabla_\perp p'_1, \tag{10}$$

$$i\alpha u'_1 + \nabla_\perp \cdot \mathbf{v}'_{\mathbf{1}\perp} = 0. \tag{11}$$

The above set of equations is further simplified by writing it in terms of the stream-function ϕ_1 for the rolls: $\overline{v}_1 = -\partial_z \phi_1$, $\overline{w}_1 = \partial_y \phi_1$, and the associated vorticity $\omega_1 = \nabla_\perp^2 \phi_1$. Taking the divergence of the fluctuation equations (9) and (10) and using the incompressibility condition (11) we obtain a Helmholtz problem for the pressure that does not involve the streamwise fluctuation u'_1. Since this quantity is also absent from the Reynolds stress term $\nabla_\perp \cdot \overline{\mathbf{v}'_{\mathbf{1}\perp}\mathbf{v}'_{\mathbf{1}\perp}}$ there is no need to solve equation (9). Lastly, the fluctuations are regularized by retaining subdominant diffusion. The reduced equations used in this paper are

therefore the following:

$$\partial_T u_0 + J(\phi_1, u_0) = \nabla_\perp^2 u_0 + \tfrac{\sqrt{2}\pi^2}{4} \sin\left(\tfrac{\pi y}{2}\right), \tag{12}$$

$$\partial_T \omega_1 + J(\phi_1, \omega_1) + 2\left(\partial_y^2 - \partial_z^2\right)(\mathcal{R}(v_1 w_1^*)) + 2\partial_y\partial_z(w_1 w_1^* - v_1 v_1^*) = \nabla_\perp^2 \omega_1, \tag{13}$$

$$\left(\alpha^2 - \nabla_\perp^2\right) p_1 = 2i\alpha\left(v_1 \partial_y u_0 + w_1 \partial_z u_0\right), \tag{14}$$

$$\partial_t \mathbf{v_{1\perp}} + i\alpha u_0 \mathbf{v_{1\perp}} = -\nabla_\perp p_1 + \epsilon\nabla_\perp^2 \mathbf{v_{1\perp}}. \tag{15}$$

In writing these equations we have dropped all overbars and primes and introduced the notation $J(\phi_1, \cdot) = \partial_y\phi_1\partial_z \cdot - \partial_z\phi_1\partial_y\cdot$. The symbol $\mathcal{R}$ denotes the real part of a complex quantity while an asterisk denotes complex conjugation. The boundary conditions associated with Waleffe flow read:

$$\partial_y u_0 = \omega_1 = \phi_1 = v_1 = \partial_y w_1 = 0 \quad \text{on} \quad y = \pm 1. \tag{16}$$

The reduced system (12)–(15) represents a simplification of the full three-dimensional Navier–Stokes system. First, the equations have been projected onto a two-dimensional spatial domain. Second, the mean equations (12) and (13) have $O(1)$ diffusion while the fluctuation equations (14) and (15) are weakly diffusive and quasilinear with respect to the fluctuations. The resulting system bears some similarity with earlier work based on critical layer theory at very large Reynolds numbers [14], but we focus here on transitional states and hence on moderate Reynolds numbers. In particular we allow the critical layer to have a finite width, hereafter called a *critical region*, by retaining a subdominant diffusion term in equation (15). This regularizing term allows us to work with an equation set that is defined on the entire two-dimensional domain while retaining the Re-dependence of the ECS through the parameter $\epsilon \equiv Re^{-1}$.

Obtaining ECS from this system is not trivial: these states are nonlinear and not

6

connected to any trivial solution. The same difficulty is encountered in the fully three-dimensional Navier–Stokes framework but the structure of the reduced system allows easier computation. The streamwise-invariant quantities evolve slowly (with T) while the fluctuations possess fast dynamics. The streaks in equations (14) and (15) can then be thought of as frozen, resulting in a linear problem for the fluctuations. The fluctuation system is then solved as an eigenvalue problem for the (fast) growth rate σ of the fluctuations, assuming that u_0 is fixed. Consequently, obtaining a good ECS guess involves a two-step iterative algorithm: selecting fluctuations with the smallest growth rate for the given u_0 and then finding the corresponding steady solution (u_0, ϕ_1) from the streamwise-averaged equations. Repeating these two steps several times while tuning the amplitude of the fluctuations enables us to adjust the growth rate σ of the fluctuations to near zero, thereby yielding a good initial condition that can be converged to stationary ECS using an appropriately designed preconditioned Newton method on the complete system (12)–(15). The resulting solution is then numerically continued in Re. A more detailed description of the method is available in [6].

3   Extended states

In this section, we compute time-independent exact solutions of the reduced system (12)–(15) with the boundary conditions (16). We choose $\alpha = 0.5$ for which the lower branch solution in plane Couette flow is only once unstable [23], and discretize the (y, z) domain using equidistributed points. Minimal meshes consist of 16 points per unit length in the wall-normal direction and $32/\pi$ points per unit length in the spanwise direction. The calculations are carried out in Fourier space and fully dealiased. For simplicity we impose the three-dimensional reflection symmetry R : $(u_0, \omega_1, \phi_1, v_1, w_1)(y, z)$ $\rightarrow (-u_0, \omega_1, \phi_1, -v_1^*, -w_1^*)(-y, -z)$, together with $\alpha \rightarrow -\alpha$.

7

3.1 Spatially periodic states

Converged ECS from the reduced system (12)–(15) have already been investigated in small periodic domains [5, 6]. For a domain of spanwise period $L_z = \pi$, these solutions take the form of canonical ECS reminiscent of the Nagata states in plane Couette flow [21]. In the asymptotically reduced model of Waleffe flow these states are formed at a saddle-node bifurcation at $Re_{sn} \approx 136$, forming upper and lower ECS branches. These solutions, together with their bifurcation diagram, are shown in figure 1. The primary difference between the lower and upper branch states lies in the $O(1)$ streaks. The lower branch streaks undulate with small amplitude around $y = 0$ as opposed to the upper branch streaks which are more pronounced, nearly spanning the entire domain. The streak deformation is the result of their interaction with $O(\epsilon)$ rolls which are generated by $O(\epsilon)$ fluctuations accumulating around the $u_0 = 0$ contour, that is, around the curve of vanishing streaks. In the nominally inviscid problem, i.e., the regime of very high Reynolds numbers, this contour corresponds to the so-called critical layer. The lower branch ECS display quasi-circular rolls, explaining the sinusoidal shape of the $u_0 = 0$ contour. As the Reynolds number is decreased toward the saddle-node, the rolls strengthen while maintaining their nearly circular shape and the undulation amplitude grows. The rolls associated with the upper branch ECS are more complex: away from the saddle-node they become bimodal with a pair of local cores replacing the single core along the lower branch. These cores gradually move apart, toward the extrema of the $u_0 = 0$ contour, considerably deforming the contour near its extrema (figure 1).

3.2 Modulated states

It is known that a number of different instabilities leading to spatial modulation can arise in large domains along branches of spatially periodic structures and in particular in the
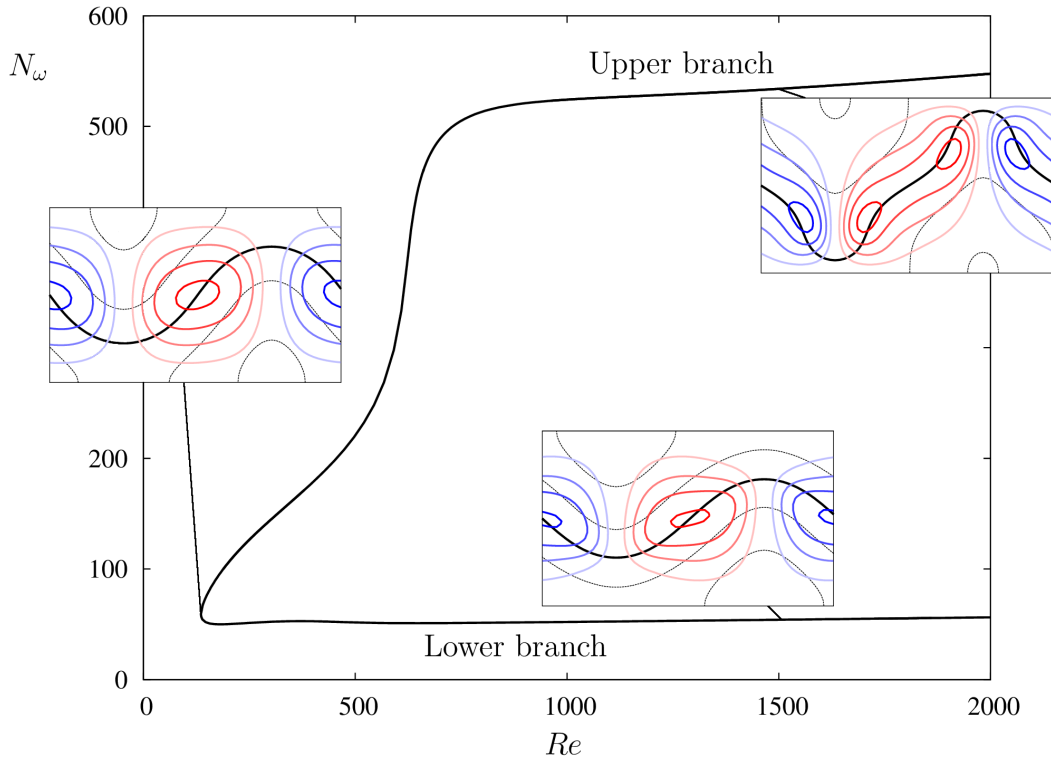
8

Figure 1: Bifurcation diagram for a domain with spanwise period $L_z = \pi$ and streamwise wavenumber $\alpha = 0.5$. The normalized enstrophy: $N_\omega = \frac{1}{D} \int_{\mathcal{D}} \omega_1^2 \, dy \, dz$ is shown as a function of the Reynolds number Re. Here $\mathcal{D}$ represents the two-dimensional domain and $D = \int_{\mathcal{D}} dy \, dz$. The insets represent the lower and upper branch states at $Re \approx 1500$ and the solution at the saddle-node $Re \approx Re_{sn}$. The thick black line represents the critical layer $u_0 = 0$, and thinner black contours are plotted for $u_0 = \pm 0.5, \pm 1$. The rolls are represented in color, with red (resp. blue) standing for positive (resp. negative) values of the streamfunction, i.e., for counter-clockwise and clockwise motion, respectively. The contours plotted are multiples of 0.4 for the lower branch state, of 0.5 for the saddle-node state and of 0.65 for the upper branch state.

9

vicinity of saddle-nodes of spatially periodic states [1, 25]. This process has been studied in detail in the context of the bistable Swift–Hohenberg equation posed on a one-dimensional domain with a large spatial period [7], and becomes analytically accessible in the context of the corresponding Ginzburg–Landau equation [15]. The resulting modulational instability may lead to the development of a hole within the spatially periodic pattern when the amplitude of modulation becomes so large that the periodic state is invaded by intervals of the trivial (laminar) state.

With this in mind, we set the domain size to $L_z = 4\pi$ and look for the formation of modulated structures at $Re \approx Re_{sn}$. The modulational instabilities described in the Swift–Hohenberg equation [7, 15] or in other fluid problems [18, 3] are linear instabilities occurring close to the saddle-node. We therefore consider the following initial conditions g_0 for our Newton method:

$$g_0 = \left[1 - \frac{\chi}{2}\left(1 + \cos\left(\frac{z}{2}\right)\right)\right] g_{per} + \left[\frac{\chi}{2}\left(1 + \cos\left(\frac{z}{2}\right)\right)\right] g_{lam}. \quad (17)$$

Here g_{per} is the spatially periodic solution at the saddle-node, g_{lam} is the homogeneous laminar solution and χ is a modulation factor. For $\chi = 0$, the initial condition is the unmodulated periodic state g_{per}; as χ increases spatial modulation with wavelength 4π (i.e., the spanwise period of the domain) of the pattern develops until $\chi = 1$ where the modulation is maximum: at $z = 0$ and $z = 4\pi$, the corresponding solution looks like the laminar profile while at $z = 2\pi$ its profile takes the form of the saddle-node solution. An example of such an initial condition is shown in figure 2 together with the exact periodic state g_{per} and the trivial laminar state g_{lam}.

To identify initial conditions that converge to a modulated state, we scanned the (Re, χ) parameter space. When the Reynolds number is too close to Re_{sn}, small values of χ generate initial conditions that are too close to the spatially periodic state and the Newton
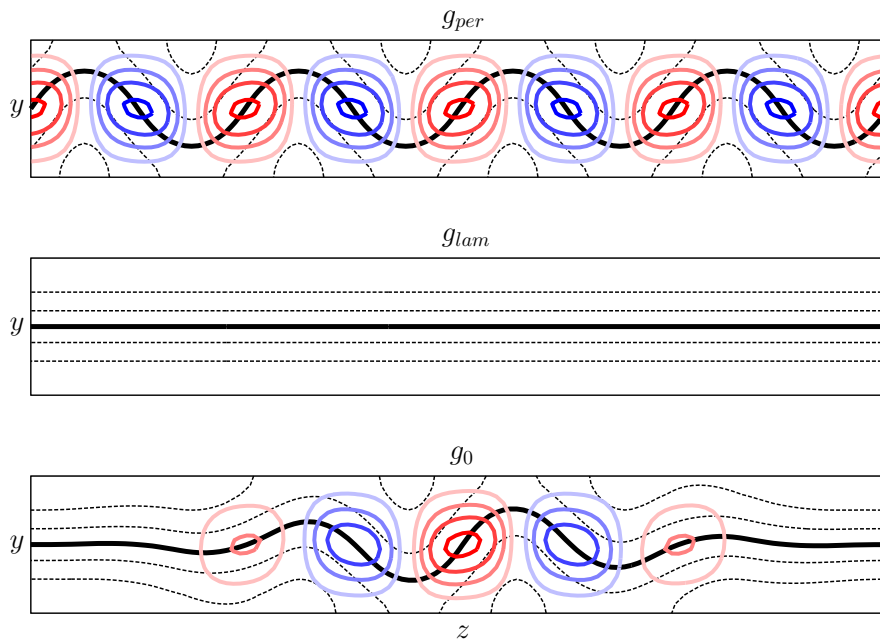
Figure 2: Relevant solutions, g_{per} and g_{lam}, used to generate the initial condition g_0 using the formula (17). The spanwise period is 4π. The solutions and initial condition are represented the same way as the saddle-node solution in figure 1. For clarity we illustrate the case $\chi = 1$.
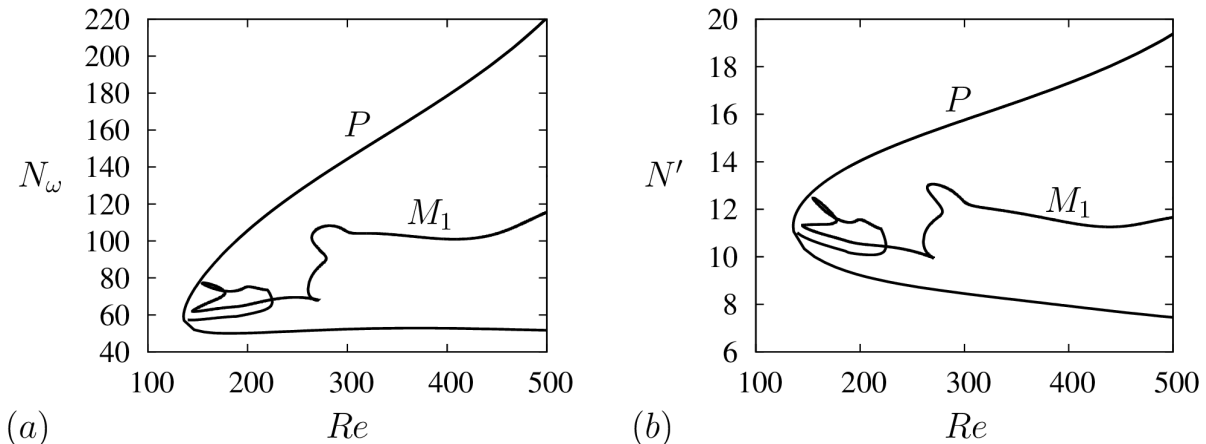
(a)

(b)

Figure 3: Bifurcation diagram for the modulated state M_1 obtained using the initial condition (17) for $Re = 140$ and $\chi = 0.2$. The quantities represented in (a) are the same as in figure 1 while a measure of the fluctuation energy $N' = \frac{1}{D}\int_{\mathcal{D}}(v_1^2 + w_1^2)\,dy\,dz$ is shown in (b). The upper branch, lower branch and saddle-node solutions of the periodic states P are shown in detail in figure 1.

iteration converges to it. However, beyond a threshold value of χ all attempts at convergence failed, the initial condition being structurally too far away from any physical state. Likewise, values of Re that were too far from Re_{sn} also failed to converge regardless of the choice of χ. However, a converged modulated state was found for $Re = 140$ and $\chi = 0.2$ and this state was then continued using our continuation algorithm [6] to trace out the branch M_1 of the corresponding solutions (figure 3). As expected, the modulated solution emerges from a bifurcation close to the saddle-node of the branch of spatially periodic states. As the solution branch is continued, the modulation of the roll amplitude (and therefore of the streaks) becomes the dominant feature (figure 4): the central (counter-clockwise) roll becomes stronger while the adjacent rolls become progressively weaker. This is particularly noticeable close to the first saddle-node of the modulated states at $Re \approx 225$. There, the ccounter-clockwise roll located at the edge of the (periodic) domain has nearly completely vanished and the adjacent clockwise rolls (in blue in figure 4) are substantially weaker, smaller and displaced from their original position (figure 4, bottom panel). To understand
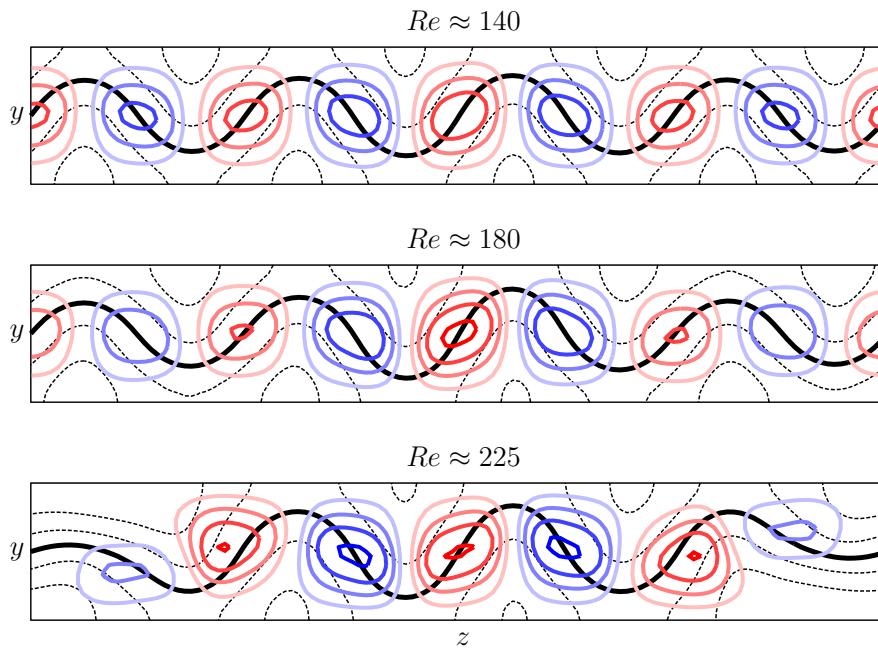
$Re \approx 140$

$Re \approx 180$

$Re \approx 225$

Figure 4: Progressive modulation of the amplitude of the modulated state as the M_1 branch departs from the vicinity of the saddle-node of the spatially periodic states. The corresponding bifurcation diagram is shown in figure 3. The solutions are represented as in figure 2 with multiples of 0.6 for the streamfunction contours.

the displacement of the weaker rolls, we substitute the fluctuation velocities from equation (15) into equation (14) and obtain:

$$\left(\alpha^2 - \nabla_\perp^2\right) p_1 = \frac{2}{u_0} \left(-\nabla_\perp p \cdot \nabla_\perp u_0 + \epsilon \nabla_\perp u_0 \cdot \nabla_\perp^2 \mathbf{v_{1\perp}}\right). \tag{18}$$

Here the term $\epsilon \nabla_\perp u_0 \cdot \nabla_\perp^2 \mathbf{v_{1\perp}}$ arises from the nature of the asymptotics performed in Section 2 but $\epsilon \nabla_\perp^2 \mathbf{v_{1\perp}}$ is never large. However, the presence of u_0 in the denominator of the right side of equation (18) is responsible for the presence of enhanced forcing of the fluctuations in the vicinity of the contour $u_0 = 0$, implying that fluctuations necessarily concentrate in the critical region, where they strengthen the rolls and in particular the counter-clockwise central roll. The weak clockwise rolls at either end deform the $u_0 = 0$ contour less, resulting in a displacement of the contour downward on the left and upward on the right (figure 4, bottom panel).

As the branch M_1 turns around towards lower values of the Reynolds number near the $Re \approx 225$ saddle-node, the clockwise rolls weaken while the counter-clockwise rolls strengthen. The resulting solution is shown in figure 5 for $Re = 155$ (top panel). At this location the M_1 branch has a saddle-node; by the next saddle-node (at $Re \approx 177$, middle panel) the central roll is starting to lose its dominance, and this evolution continues towards the leftmost saddle-node (at $Re \approx 145$, bottom panel) resulting in a roll pattern with a rather weak but nonetheless complex modulation structure characterized by a weaker central roll embedded between a pair of stronger counter-rotating rolls on either side. This modulation structure strengthens and by the next saddle-node at $Re \approx 271$ a fully-developed double-well modulation is present, centered on the roll pairs on either side of the counter-clockwise central roll (figure 6). The modulation strenghens the roll pairs on either side of the central roll while progressively weakening the central roll; this evolution generates a pair of strong streaks (see eg. figure 6, middle panel) while broadening the
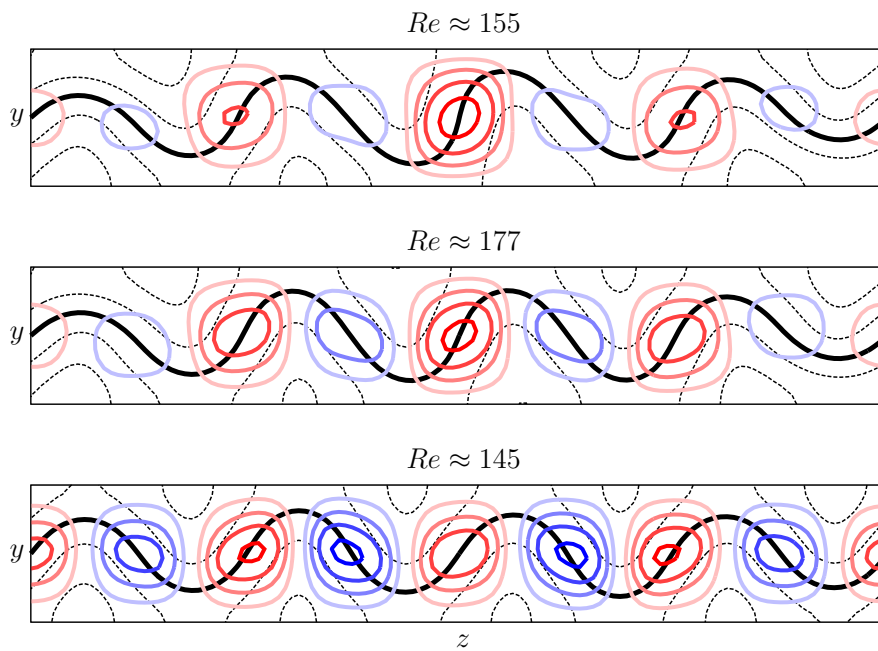
Figure 5: Evolution of the M_1 branch after its first saddle-node at $Re \approx 225$. From top to bottom: solutions at successive saddle-nodes until the leftmost saddle-node at $Re \approx 145$. The corresponding bifurcation diagram is shown in figure 3. The solutions are represented as in figure 2 with, from top to bottom, multiples of 0.95, 0.75 and 0.55 for the stream-function contours.
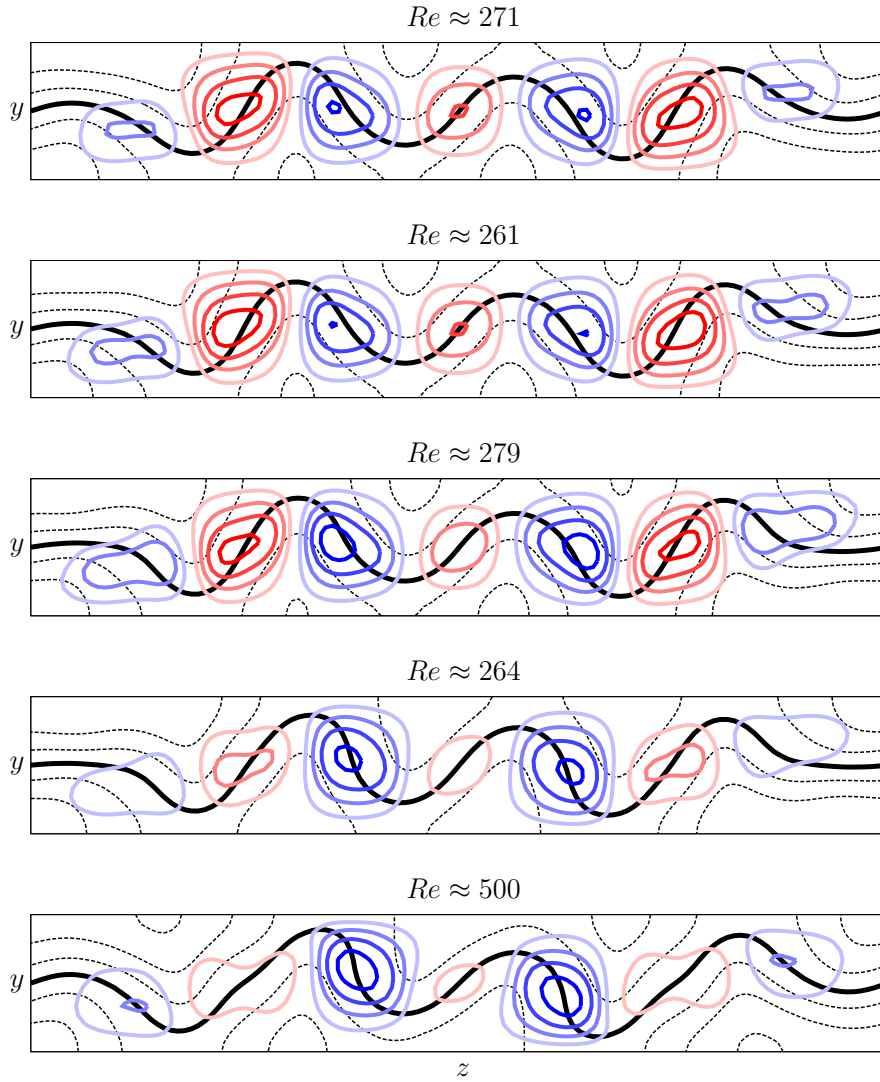
Figure 6: Evolution of the M_1 states after their approach to the periodic state (see figure 5). The solutions are shown, from top to bottom, at the four successive saddle-nodes between $Re = 250$ and $Re = 300$, starting from the one of least energy; the final solution is taken at $Re \approx 500$. The corresponding bifurcation diagram is shown in figure 3. The solutions are represented as in figure 2 with multiples of 0.6 for the streamfunction contours except for the $Re \approx 264$ and $Re \approx 500$ solutions for which the contours are multiples of 0.9.
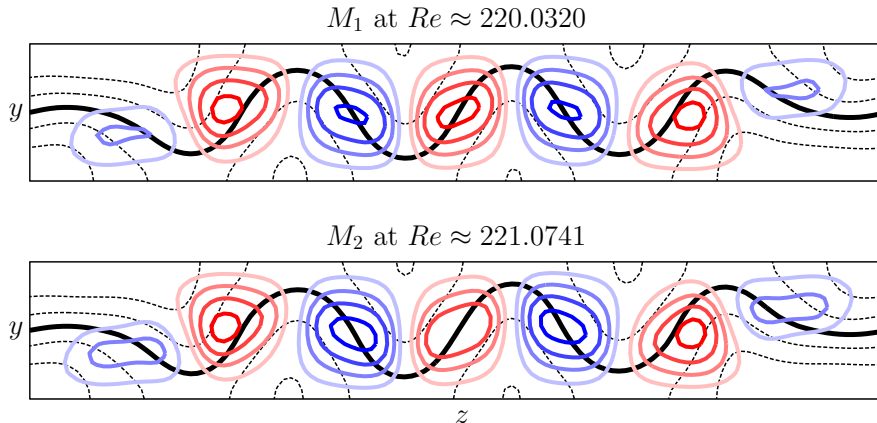
M_1 at $Re \approx 220.0320$

M_2 at $Re \approx 221.0741$

Figure 7: Nearby M_1 and M_2 solutions represented as in previous figures with streamfunction contours that are multiples of 0.6. These solutions are indicated with a solid dot in the corresponding bifurcation diagram shown in figure 8.

weak clockwise structures towards the outside. The next saddle-node on the left reveals the presence of dramatic weakening of the outer counter-clockwise rolls while the inner clockwise rolls strengthen resulting in the steeping of the $u_0 = 0$ contour within the latter, a process that is progressively enhanced as Re increases (figure 6, bottom panel), in a manner suggestive of incipient roll-up. The fold at $Re \approx 145$ is therefore responsible for the splitting of the one-pulse state into two pulses. Similar splitting of a single-pulse localized structure occurs in rotating convection [4].

While tracking the M_1 state in figure 3, we noticed the presence of a (well-resolved) sharp angle in the direction of the branch at $Re \approx 220$ in all the quantities we monitored. This type of event might indicate an imperfect bifurcation and therefore the existence of another branch nearby with similar solutions. We initialized a Newton search with an M_1 solution at $Re \approx 220.0320$ and slightly perturbed it by increasing its amplitude and the Reynolds number. Using this procedure we were able to converge to another kind of modulated state, labelled M_2. The M_1 solution we picked together with the M_2 state we converged to are represented in figure 7 to illustrate the similarities and differences between them, with the associated bifurcation diagram displayed in figure 8. The full
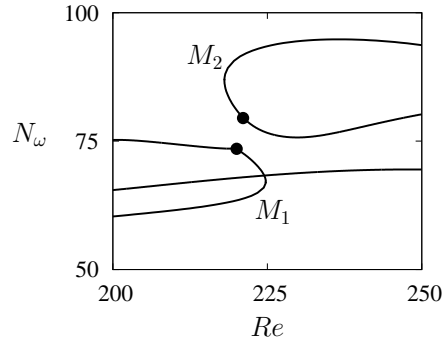
Figure 8: Close-up of the region where the M_1 and M_2 states approach each other. The solution on M_1 indicated by the solid dot was used to converge to the M_2 solution also indicated by a solid dot.
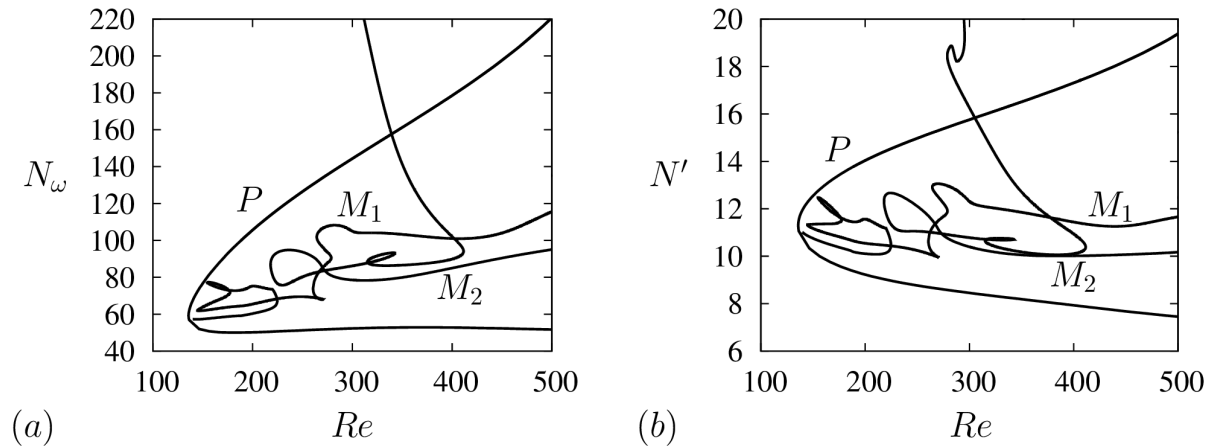

Figure 9: Bifurcation diagram for the modulated states M_1 and M_2. The quantities represented are the same as in figure 3.

bifurcation diagram of the M_2 states is shown in figure 9. Continuation of the modulated states M_2 shows that these states are created at a saddle-node at $Re \approx 218$. The upper and lower branches emanating from this saddle-node then have completely different fate. The upper M_2 branch evolves monotonically to larger Reynolds numbers while the modulation of the amplitude of the rolls increases and the size of the central roll decreases. This simple evolution is shown in figure 10. The lower branch has a more complex structure, however. Along this branch the central counter-clockwise roll gradually weakens and then splits into two maxima in the vicinity of the center of the domain. At the same time the
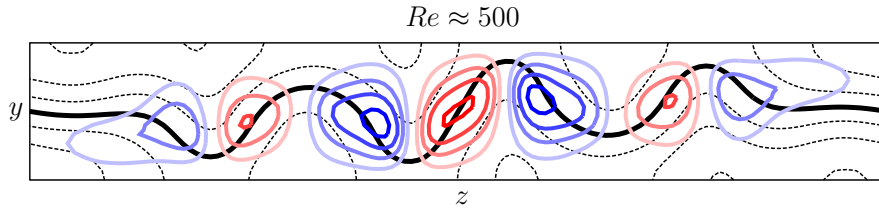
18

$Re \approx 500$

Figure 10: Solution taken along the upper M_2 branch at $Re \approx 500$. The corresponding bifurcation diagram is shown in figure 9. The solution is represented as in figure 2 with multiples of 0.6 for the streamfunction contours.

remaining counter-clockwise rolls also weaken leaving a structure dominated by a pair of strong clockwise rolls. This process manifests itself in the presence of a small loop between $Re \approx 315$ and $Re \approx 342$ and terminates near the $Re \approx 411$ saddle-node in figure 11. The branch then turns around and both N and N' increase dramatically. During this process the two clockwise rolls near the center of the domain that dominate the flow at $Re \approx 411$ are swamped by the growth of a pair of clockwise rolls near either side of the domain and the associated elimination of counter-clockwise rolls from all but the center of the domain where a weak counter-clockwise roll persists. It is significant that the new clockwise rolls that appear are no longer centered on the $u_0 = 0$ contour. This appears to be a consequence of their proximity in a domain with periodic boundary conditions and of the resulting roll-up. This incipient roll-up may in turn be responsible for the dramatic increase in roll and fluctuation energies observed in figure 9. This behavior hints at a possible failure of the asymptotic approach in this regime, although we have not pushed the calculations into this regime. We reiterate that all the solutions reported here are fully converged.
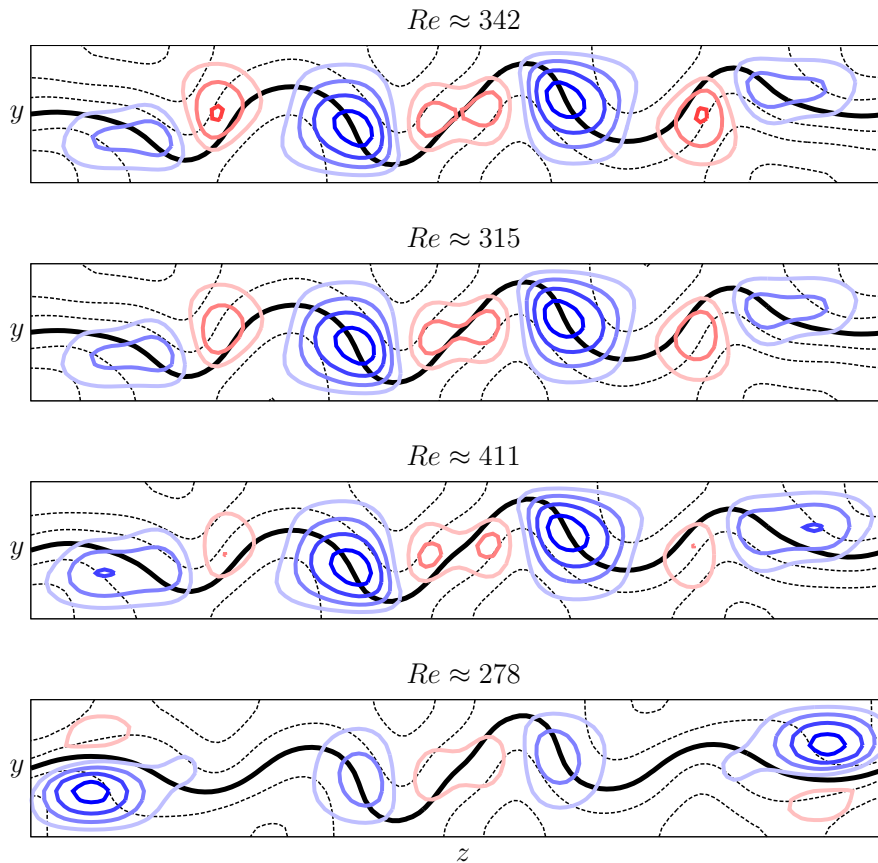
$Re \approx 342$

$Re \approx 315$

$Re \approx 411$

$Re \approx 278$

Figure 11: Solutions along the lower M_2 branch at successive saddle-nodes at $Re \approx 342$, $Re \approx 315$, $Re \approx 411$ and $Re \approx 278$. The corresponding bifurcation diagram is shown in figure 9. The solution is represented as in figure 2 with multiples of 0.7 for the stream-function contours, except for the $Re \approx 278$ saddle-node where multiples of 1.2 have been used.

4 Conclusion

In this paper, we have obtained and numerically continued the first spanwise-modulated states in a reduced model of parallel shear flow, focusing on time-independent solutions with the symmetry R. These states were found using insight from pattern-forming systems: the saddle-node of subcritical spatially periodic states in extended systems is known to give rise to modulational instabilities. We constructed an artificial modulation of the saddle-node solution and converged it to a modulated state referred to as M_1 that we have successfully continued to unveil a complex bifurcation structure reminiscent of fully three-dimensional shear flows [22, 12, 19]. Additional solutions such as the M_2 modulated states were identified by perturbing the M_1 state close to what looks like an imperfect bifurcation, and these were likewise continued numerically to substantially different Reynolds numbers. We mention that states with a shift-reflect symmetry, corresponding to a cross-stream reflection followed by a half wavelength shift in the streamwise direction, are also expected to be present [24, 6]. Such solutions are not stationary, however, but drift steadily in the streamwise direction, i.e., they are traveling waves. We have not computed traveling states of this type.

The reduced model used for this purpose has been derived based on the scaling properties of the lower branch state observed in plane Couette flow [29]. The resulting equations are in effect projected in the streamwise direction on the fundamental and first Fourier components of the velocity and pressure fields but spanwise and wall-normal directions are treated as in fully simulated flows. As a result, 3 real fields (u_0, ω_1 and ϕ_1) and 3 complex fields (p_1, v_1 and w_1) have to be solved for on a $N_y \times N_z$ mesh, where N_y (resp. N_z) stands for the number of points in the wall-normal (resp. spanwise) direction. The computation of such states using a direct numerical solver on the primitive equations typically involves 4 real fields – the three components of the velocity and the pressure – on a $N_x \times N_y \times N_z$ mesh

with $N_x = O(10)$ at least [23, 12, 19]. The calculations presented here would therefore have been at least 10 times slower had a fully three-dimensional solver been used. Additional difficulties arise in the Newton iteration as the number of degrees of freedom increases.

The finding of the modulated states M_1 and M_2 in a reduced model has several implications for transitional shear flows. It shows that the reduced model (12)–(15), originally designed to capture the lower branch solutions, not only captures the upper branch states, but also bifurcations from these states and even more complex, unconnected states. This property of the reduced model is expected to provide substantial help in the systematic study of both extended and spatially localized ECS [24]. In the present study no ECS localized in the spanwise direction were found but some of the modulated states strongly suggest that spanwise-localized modulated states do, in fact, exist although no homoclinic snaking was observed. The M_1 and M_2 states nearly coincide in an imperfect bifurcation around $Re = 220$. Had they connected their connection would have given rise to a branch starting from the saddle-node of the periodic states, spending some time around $Re = 220$, before extending monotonically to large Reynolds numbers and resulting in solutions consisting of a spatially modulated roll pattern with a simple structure. Similar modulated states that do not snake but instead extend monotonically to large parameter values have been found in Marangoni convection [1] and studied in detail in the context of binary fluid convection [20]. These studies, in conjunction with earlier studies of model equations such as the Swift–Hohenberg equation [7, 9], indicate that in finite domains the behavior of branches of modulated structures is strongly affected by the spanwise spatial period imposed on the system, suggesting that for a different choice of this period homoclinic snaking may in fact be present in the reduced shear flow model studied here. This is particularly so for moderately large domains, such as $L_z = 4\pi$, as used here. However, despite this limitation, the present study serves as a proof of concept that reduced models, such as that consisting of equations (12)–(15), do capture more dynamics than they have

been designed for, thereby paving the way for future studies on larger domains at lesser computational cost.

References

[1] P. Assemat, A. Bergeon and E. Knobloch, Fluid Dyn. Res., 40 (2008) 852–876

[2] C. Beaume, Proc. Geophysical Fluid Dynamics Program, Woods Hole Oceanographic Inst. (2012) 389–412

[3] C. Beaume, E. Knobloch and A. Bergeon, Phys. Fluids, 25 (2013) 114102

[4] C. Beaume, E. Knobloch and A. Bergeon, Phys. Fluids, 25 (2013) 124105

[5] C. Beaume, E. Knobloch, G. P. Chini and K. Julien, Fluid Dyn. Res., 47 (2015) 015504

[6] C. Beaume, G. P. Chini, K. Julien and E. Knobloch, Phys. Rev. E, 91 (2015) 043010

[7] A. Bergeon, J. Burke, E. Knobloch and I. Mercader, Phys. Rev. E, 78 (2008) 046201

[8] M. Chantry, L. S. Tuckerman and D. Barkley, arXiv:1506.05002 (2015)

[9] J. H. P. Dawes, SIAM J. Appl. Dyn. Syst., 8 (2009) 909–930

[10] P. G. Drazin and W. H. Reid, Hydrodynamic Stability, Cambridge University Press (1981)

[11] Y. Duguet, P. Schlatter and D. S. Henningson, Phys. Fluids, 21 (2009) 111701

[12] J. F. Gibson, J. Halcrow, and P. Cvitanović, J. Fluid Mech., 638 (2009) 243–266

[13] P. Hall and F. T. Smith, J. Fluid Mech., 227 (1991) 641–666

[14] P. Hall and S. J. Sherwin, J. Fluid Mech., 661 (2010) 178–205

[15] H.-C. Kao and E. Knobloch, Phys. Rev. E, 85 (2012) 026211

[16] G. Kawahara and S. Kida, J. Fluid Mech., 449 (2001) 291–300

[17] G. Kawahara, M. Uhlmann and L. van Veen, Annu. Rev. Fluid Mech., 44 (2012) 203–225

[18] D. Lo Jacono, A. Bergeon and E. Knobloch, Phys. Fluids, 22 (2010) 073601

[19] K. Melnikov, T. Kreilos and B. Eckhardt, Phys. Rev. E, 89 (2014) 043008

[20] I. Mercader, O. Batiste, A. Alonso and E. Knobloch, J. Fluid Mech., 667 (2011) 586–606

[21] M. Nagata, J. Fluid Mech., 217 (1990) 519–527

[22] A. Schmiegel, PhD dissertation, Marburg University (1990)

[23] T. M. Schneider, J. F. Gibson, M. Lagha, F. de Lillo and B. Eckhardt, Phys. Rev. E, 78 (2008) 037301

[24] T. M. Schneider, J. Gibson and J. Burke, Phys. Rev. Lett., 104 (2010) 104501

[25] T. M. Schneider, D. Marinc and B. Eckhardt, J. Fluid Mech., 646 (2010) 441–451

[26] G. I. Taylor, Phil. Trans. R. Soc. Lond. A, 223 (1923) 289–343

[27] F. Waleffe, Phys. Fluids, 9 (1997) 883–900

[28] F. Waleffe, J. Fluid Mech., 435 (2001) 93–102

[29] J. Wang, J. Gibson and F. Waleffe, Phys. Rev. Lett., 98 (2007) 204501